

1 **Holocene Asian monsoon evolution revealed by a pollen record from**
2 **an alpine lake on the southeastern margin of the Qinghai-Tibetan**
3 **Plateau, China**

4 **E. Zhang¹, Y. Wang², W. Sun^{1,3}, and J. Shen¹**

5 ¹State Key Laboratory of Lake Science and Environment, Nanjing Institute of Geography and Limnology, Chinese
6 Academy of Sciences, Nanjing 210008, China

7 ²College of Resource Environment and Tourism, Capital Normal University, Beijing 100048, China

8 ³University of Chinese Academy of Sciences, Beijing 100049, China

9 **Correspondence to: E. Zhang (elzhang@niglas.ac.cn); J. Shen (jishen@niglas.ac.cn)**

10 **Abstract**

11 We present the results of pollen analyses from a 1105-cm-long sediment core from Wuxu Lake in
12 southwestern China, which depict the variations of the East Asian winter monsoon (EAWM) and the Indian
13 summer monsoon (ISM) during the last 12.3 ka. During the period of 12.3 to 11.3 cal ka BP, the dominance of
14 *Betula* forest and open alpine shrub and meadow around Wuxu Lake indicates a climate with relatively cold
15 winters and dry summers, corresponding to the Younger Dryas event. Between 11.3 and 10.4 cal ka BP, further
16 expansion of *Betula* forest and the retreat of alpine shrubs and meadows reflect a greater seasonality with cold
17 winters and gradually increasing summer precipitation. From 10.4 to 4.9 cal ka BP, the dense forest understory,
18 together with the gradual decrease in *Betula* forest and increase in *Tsuga* forest, suggest that the winters became
19 warmer and summer precipitation was at a maximum, corresponding to the Holocene climatic optimum. Between
20 4.9 and 2.6 cal ka BP, *Tsuga* forest and alpine shrubs and meadows expanded significantly, reflecting relatively
21 warm winters and decreased summer precipitation. Since 2.6 cal ka BP, reforestation around Wuxu Lake indicates
22 a renewed humid period in the late Holocene; however, the vegetation in the catchment may also have been
23 affected by grazing activity during this period. The results of our study are generally consistent with previous
24 findings; however, the timing and duration of the Holocene climatic optimum from different records are
25 inconsistent, reflecting real contrast in local rainfall response to the ISM. Overall, the EAWM is broadly in-phase
26 with the ISM on the orbital timescale, and both monsoons exhibit a trend of decreasing strength from the early to

27 late Holocene, reflecting the interplay of solar insolation receipt between the winter and summer seasons and El
28 Niño Southern Oscillation strength in the tropical Pacific.

29 **Keywords:** Holocene; Asian monsoon; pollen assemblages; Wuxu Lake; southwestern China

30

31 **1. Introduction**

32 As an important component of the global climate system, the Asian summer monsoon, including Indian and
33 East Asian summer monsoon systems, significantly affects sustainable development and ecosystem dynamics
34 within a large, densely populated region (An et al., 2000). During the last two decades, the variability of the Indian
35 summer monsoon (ISM) in the Holocene has been reconstructed from various types of paleoclimatic archive and
36 proxies, such as stalagmite oxygen isotope ($\delta^{18}\text{O}$) records (Cai et al., 2012; Fleitmann et al., 2007; Fleitmann et al.,
37 2003), marine sediments (Contreras-Rosales et al., 2014; Gupta et al., 2003; Rashid et al., 2007), and lake and
38 peatland sediments (Bird et al., 2014; Chen et al., 2014; Cook et al., 2013; Demske et al., 2009; Fuchs and
39 Buerkert, 2008; Jarvis, 1993; Kramer et al., 2010; Prasad et al., 2014; Sarkar et al., 2015; Shen et al., 2006a; Shen
40 et al., 2006b; Shen et al., 2005; Song et al., 2012; Sun et al., 2015; Xiao et al., 2014a). Among the numerous
41 records, stalagmites can be accurately and precisely dated using U-series methods (Cheng et al., 2000). The
42 stalagmite $\delta^{18}\text{O}$ results from various sites indicate a uniform evolution history with the optimum climate occurring
43 in the early Holocene. However, stalagmite $\delta^{18}\text{O}$ values are also influenced by seasonality of precipitation,
44 moisture source and transport pathway, especially in eastern China (Breitenbach et al., 2010; Maher, 2008; Maher
45 and Thompson, 2012; Pausata et al., 2011; Tan, 2014; Wang et al., 2001). In contrast, the timing and duration of
46 the Holocene climatic optimum inferred from marine and lake sediment records differ from the speleothem record,
47 possibly because of differences in temporal resolution, in the sensitivity of the proxy, and the lack of reliable
48 chronologies (Hou et al., 2012; Sun et al., 2015; Zhang et al., 2011). In addition, there is also the potential of local
49 differences in ISM precipitation response (Bird et al., 2014), and therefore there is a need for additional detailed
50 paleoclimatic studies in the region.

51 The East Asian winter monsoon (EAWM), which originates in the Siberian high centered in Mongolia and
52 northeastern Siberia, is the winter counterpart of the Asian summer monsoon in China and is characterized by cold
53 and dry northwesterly or northeasterly winds (Chen et al., 2000). However, high-resolution records of the EAWM
54 for the Holocene are sparse and their interpretation is controversial. Records of Ti concentration, total organic

55 carbon content and magnetic susceptibility from Huguangyan Lake in southern China suggest a strengthening of
56 the EAWM from the early to the late Holocene (Yancheva et al., 2007); however, geochemical and magnetic
57 analyses indicate that the local pyroclastic bedrock is the dominant source of the Huguangyan Lake sediments
58 (Shen et al., 2013; Zhou et al., 2009). In addition, recent studies, based on diatom assemblages and stable nitrogen
59 isotope ($\delta^{15}\text{N}$) analyses of sediments from the same lake, indicate a stronger EAWM in the early Holocene (Jia et
60 al., 2015; Wang et al., 2012). Other proxies for reconstructing Holocene EAWM variability include the grain size
61 distribution of loess deposits and thermocline gradients from the South China Sea, although are of low temporal
62 resolution (Huang et al., 2011; Steinke et al., 2011; Steinke et al., 2010; Stevens et al., 2007; Sun et al., 2012; Tian
63 et al., 2010).

64 Southwestern China, which mainly includes the Yunnan-Guizhou Plateau, the Sichuan Basin and the
65 southeastern Qinghai-Tibetan Plateau (QTP), is a typical region which is strongly influenced by the ISM and
66 EAWM (An et al., 2000). Modern pollen data indicate that the mean temperature of the coldest month and annual
67 precipitation are the dominant climatic variables of modern pollen/vegetation distributions in South China (Li et al.,
68 2015). Pollen analysis has been widely used to reconstruct Holocene paleovegetation and paleoclimate in the
69 region (Chen et al., 2014; Cook et al., 2013; Jarvis, 1993; Kramer et al., 2010; Shen et al., 2006a; Shen et al.,
70 2006b; Song et al., 2012; Xiao et al., 2014a). However, in most of these records the chronology is based on
71 radiocarbon dating of bulk organic matter and/or is of low resolution.

72 Wuxu Lake is an alpine lake in the mountainous region of the southeastern QTP. The altitude is about 3706 m
73 a.s.l. (Xiao et al., 2012), and close to the elevation of the present tree-line in the region, which increases the
74 sensitivity of vegetation to climate change. Here we present a Holocene pollen record from the lake sediments, and
75 use it to reconstruct the history of regional vegetation and climate changes, and thus the evolution of the ISM and
76 EAWM.

77

78 **2. Study Site**

79 Wuxu Lake (29°9'11.48"N, 101°24'21.6"E) is located in an eastern branch of the Hengduan Mountains on the
80 southeastern margin of the QTP (Fig. 1a). The southeastern margin of the QTP is characterized by steep
81 valley-ridge relief, characterized by parallel, deep and narrowly incised river valleys such as Dadu River, Yalong
82 River and Jinsha River. The elevation ranges from 1500 m asl to above 5000 m asl, resulting in steep climatic

83 gradients in the region. Mean summer (from June to August) temperature ranges from 5 to 21 °C, and mean annual
84 precipitation varies between 500 and 1200 mm (Yu et al., 2001). The regional vegetation includes warm temperate
85 evergreen broad-leaved forest in the foothills, cool evergreen coniferous forest extending up to 4400m a.s.l., and
86 alpine shrubs and meadows in the cold, high-elevation regions below the permanent snowline (Wu et al., 1980).

87 Wuxu Lake has an area of 0.5 km² with a catchment area of 6.5 km² (Wischnewski et al., 2011). The
88 maximum water depth is 30.8 m (Wischnewski et al., 2011). The lake is fed mainly by a single stream which enters
89 on the northwest side of the lake and has a single outflow in the southeast, which flows into the Jiulong River and
90 then into the Yalong River (Fig. 1b). The closest weather station is Litang Station at 3948 m asl, which records a
91 mean July temperature of 10.5 °C, mean January temperature of -6 °C, and mean annual precipitation of 720 mm
92 which mainly occurs in the rainy season from May to September (Wischnewski et al., 2011). The vegetation
93 around the lake is dominated by *Picea likiangensis*, *Abies squamata*, *Quercus aquifoliodes* and *Quercus pamosa*
94 with *Betula utilis*, *Betula platyphylla*, *Salix* and *Rhododendron* occurring in the secondary canopy. The forest is
95 gradually replaced by subalpine *Rhododendron* shrubs and alpine meadows with increasing altitude. At present the
96 catchment is little disturbed by human activity. Occasionally, Tibetan yak herdsman use the area as grazing
97 grounds during summer.

98

99 **3. Materials and methods**

100 **3.1 Sediment sampling and dating**

101 In summer 2010, we obtained a 1105-cm-long sediment core from the deepest part of Wuxu Lake (30-m
102 depth) using a UWITEC piston corer. The core was sub-sampled at 1-cm contiguous intervals and stored at 4 °C
103 prior to analysis. The chronology is based on accelerator mass spectrometry (AMS) ¹⁴C dates from terrestrial plant
104 macrofossils extracted from the sediment samples. The analyses were made by Beta Analytic Inc. in Miami, USA
105 and the Rafter Radiocarbon Laboratory in the Institute of Geological and Nuclear Sciences, New Zealand. All of
106 the 18 AMS ¹⁴C dates obtained were calibrated to calendar years before present (0 BP=1950 AD) using the
107 program Calib 7.1 and the IntCal13 calibration data set (Reimer et al., 2013).

108 **3.2 Pollen analysis**

109 Samples for pollen analysis were determined at 4-cm intervals and treated using standard laboratory methods

110 (Fægri et al., 1989), including treatment with HCl and HF to remove carbonate and silicate, boiling in KOH to
111 remove humic acid, sieving with 10µm and 120 µm mesh clothes to remove the fine and coarse fractions,
112 respectively; and mounting in silicone oil. Prior to these treatments, tablets containing a known quantity of
113 *Lycopodium* spores were added to each sample in order to determine the pollen concentration. At least 500
114 terrestrial pollen grains per sample were counted. The percentage for each pollen type was calculated based on the
115 sum of total terrestrial pollen; pollen and spores from aquatic plants and ferns were excluded from the calculation.

116 **3.3 Data treatment and statistical analyses**

117 The pollen diagram was divided into biostratigraphic zones based on constrained incremental sum of squares
118 (CONISS) using the Tilia program (Grimm, 1987). CONISS uses an algorithm based on
119 stratigraphically-constrained chord-distance clustering and square-root transformation of the pollen percentage
120 data. Only pollen taxa with a representation >1% in at least two samples were included in the zonation.

121 In order to identify and visualize the main directions of vegetation change, 31 terrestrial pollen types with a
122 representation >1% in at least two samples were included in an ordination analysis. *Pinus* pollen is considered to
123 be transported from the lowest altitude vegetation zone in the region, or from long distance sources. Its percentage
124 values are the highest of all of the taxa recorded and they do not exhibit any obvious change; therefore, its
125 weighting was set to 0.1 in the numerical analysis (Xiao et al., 2014a). Detrended Correspondence Analysis (DCA)
126 yielded gradients of 1.03 standard deviations for the pollen dataset, indicating that linear-based methods such as
127 Principal Component Analysis (PCA) are appropriate for the dataset. The PCA analysis was applied to the
128 square-root-transformed pollen data for inter-species correlations. The DCA and PCA analyses were performed
129 using the CANOCO program 4.5 (ter Braak and Šmilauer, 2002).

130

131 **4. Results and interpretation**

132 **4.1 Chronology**

133 The results of AMS ¹⁴C radiocarbon dating of the Wuxu Lake plant remains are shown in Table 1. The results
134 indicate a roughly linear age-versus-depth relationship and therefore that the sediment accumulation rate was
135 relatively constant. A Bayesian model, taking the sediment accumulation rates into account (Blaauw and Andres
136 Christen, 2011), was used to construct the age-depth model (Fig. 2) The model was determined using the default

137 settings for lake sediments at 10-cm intervals implemented using the statistical software package R (R
138 Development Core Team, 2013). The basal age is about 12.3 cal ka BP, yielding an average sediment
139 accumulation rate of 89.5 cm ka⁻¹, and thus the average temporal sampling resolution is about 45 years for the
140 pollen record.

141 **4.2 Pollen assemblages**

142 A total of 214 pollen and spore types were identified, including 118 arboreal taxa, 40 herbaceous taxa and 20
143 fern taxa. The entire pollen record is dominated by arboreal taxa, including *Pinus*, sclerophyllous *Quercus*,
144 *Picea/Abies* and *Betula*, with contributions of *Alnus*, *Tsuga*, *Lithocarpus/Castanea*, Cupressaceae, deciduous
145 *Quercus* and Ericaceae. The average percentage of the main herbaceous taxa, including *Artemisia*, Gramineae,
146 Rosaceae, Ranunculaceae, *Thalictrum*, Labiatae, Gesneriaceae and Cyperaceae, is 18.4%. The pollen spectra can
147 be divided into five assemblage zones according to the changes in terrestrial pollen percentages (Fig. 3).

148 In Zone I (12.3- 11.3 cal ka BP), arboreal taxa account for more than 70% of total terrestrial pollen, among
149 which *Pinus*, sclerophyllous *Quercus* and *Betula* predominate. Other common taxa include deciduous *Quercus*,
150 *Picea/Abies*, *Carpinus*, Gramineae, *Artemisia*, Ranunculaceae, Cyperaceae and *Thalictrum*. The zone is also
151 characterized by the high abundance of herbaceous taxa, including *Artemisia*, Cyperaceae, Gramineae and
152 *Thalictrum*, which all exhibit highest percentages throughout the entire record. *Carpinus* and *Picea/Abies* maintain
153 at high abundances within the zone, while *Betula* exhibits a generally increasing trend.

154 . A notable feature of Zone II (11.3-10.4 cal ka BP) is the abrupt decrease in herbaceous taxa to the benefit of
155 arboreal taxa. *Artemisia* and Cyperaceae fall from 10% to 5%, and Gramineae and *Thalictrum* from 5 to 2%,
156 respectively. *Betula* reaches its maximum (generally over 20%) for the entire record. *Pinus*, *Picea/Abies* and
157 *Carpinus* exhibit similar percentages as in zone I.

158 The third zone (Zone III, 10.4-4.9 cal ka BP) is characterized by relative high arboreal pollen percentages of
159 the entire record and is divided into three sub-zones:

160 *Sub-zone III-1 (10.4-8.2 cal ka BP)*: The percentages of total arboreal and herbaceous pollen are relatively
161 constant; however, *Tsuga* begins to be continuously represented in the pollen spectra. Shrub taxa such as
162 Actinidiaceae and *Rubus* increase significantly, while Rosaceae, *Potentilla*, Gesneriaceae, Labiatae and *Hypericum*
163 increase slightly. *Betula*, *Thalictrum* and Cyperaceae decrease gradually.

164 *Sub-zone III-2 (8.2-6.6 cal ka BP)*: Herbaceous taxa increase compared to the previous sub-zone, generally
165 resulting from increases in *Artemisia*, *Thalictrum*, Ranunculaceae and Cyperaceae. The representation of *Carpinus*
166 and deciduous *Quercus* are similar to the previous sub-zone. *Betula* is gradually replaced by sclerophyllous
167 *Quercus*, which is the dominant arboreal taxon. *Picea/Abies* decreases slightly from 5 to 2%, while *Tsuga* and
168 Taxodiaceae/Cuperessaceae exhibit a minor increase.

169 *Sub-zone III-3 (6.6- 4.9 cal ka BP)*: Sclerophyllous *Quercus* increases slightly at the expense of *Betula*,
170 Taxodiaceae/Cuperessaceae and *Picea/Abies*. Actinidiaceae and *Rubus* return to relatively high values. The
171 percentages of total arboreal pollen increases slightly compared to the previous sub-zone.

172 The contribution of herbaceous taxa in Zone IV (4.9-2.6 cal ka BP) increases up to 30%, as the result of
173 higher percentages of *Artemisia*, Cyperaceae, Gramineae. Arboreal taxa decrease to around 70%, mainly due to the
174 reduced *Betula* and deciduous *Quercus*. *Tsuga* percentages are the highest in the entire record, and Ericaceae and
175 *Hippophae* increase significantly. There is a slight increase in the representation of *Picea/Abies*, *Alnus* and
176 *Carpinus*.

177 Overall, the pollen spectra in Zone V (after 2.6 cal ka BP) are similar to those of Zone IV, but with a slightly
178 increased representation of arboreal taxa. *Betula* continues to decrease, *Carpinus* and *Tsuga* decrease slightly, and
179 sclerophyllous and deciduous *Quercus* increase slightly, to up to 20% and 5%, respectively. But Rosaceae,
180 *Potentilla*, Gesneriaceae, Labiatae and *Hypericum* increase slightly, while *Artemisia*, Cyperaceae, Gramineae and
181 Ranunculaceae decrease slightly. It is noteworthy that *Sanguisorba* increases significantly in this zone.

182 **4.3 Ordination analysis**

183 The PCA analysis, based on 31 terrestrial pollen taxa from 276 samples, indicates that the first two axes
184 capture 45.8% of the total variance, with the first PCA component capturing over 33.7% (Fig. 4a). Three
185 assemblages can be distinguished: alpine shrubs and meadows characterized by Cyperaceae, *Artemisia*,
186 *Polygonum*, *Thalictrum*, Ranunculaceae, *Ericaceae*, *Hippophae* and *Salix* (in the top left quadrant); cool-cold mixed
187 forest characterized by *Abies/Picea*, *Betula*, *Carpinus* and deciduous *Quercus* (in the top right quadrant); and
188 temperate mixed forest characterized by sclerophyllous *Quercus*, *Tsuga*, *Alnus*, *Lithocarpus/Castanopsis*, *Rubus*
189 and Actinidiaceae (in the bottom left quadrant). The ordination of pollen taxa along the first PCA axis apparently
190 reflects a transition from warm to cold winter temperature, since cold-tolerant taxa such as *Abies/Picea*, *Betula* and
191 other deciduous broadleaved taxa are located on the positive side, while *Tsuga*, which is sensitive to winter

192 temperature and annual temperature range, is on the negative side (An et al., 2011; Li et al., 2015). The
193 arrangement of the pollen taxa along the second axis separates the major alpine shrub and meadow taxa from the
194 forest taxa, reflecting the degree of openness of the vegetation communities, and can be interpreted as representing
195 a change from dry to more humid conditions. The PCA separates the samples into approximately five groups (Fig.
196 4b), which generally correspond to the defined pollen zones of the sequence. Samples of zones I, II and III have
197 moderate to high positive scores on the first axis, while samples of zone IV and V have negative scores. Samples
198 of zones I, II and V have high scores on the second axis, while samples of zone III and V have low scores. Spectral
199 analysis was conducted on the PCA axis 2 sample scores using the program REDFIT38 (Schulz M and Mudelsee
200 M, 2002), and revealed periodicities of 110-, 106- and 93-years (significant at the >90% confidence level) (Fig. 5).

201

202 **5. Discussion**

203 **5.1 Holocene vegetation and climate evolution**

204 Given the close proximity of Wuxu Lake to the modern tree-line, the vegetation around the catchment should
205 react sensitively to climate change. However, lake surface pollen assemblages from the region indicate that large
206 amounts of arboreal pollen, including *Pinus*, *Picea/Abies*, *Betula*, deciduous *Quercus*, *Tsuga* and evergreen
207 *Quercus* from the lower vegetation zones, are introduced into subalpine and alpine lakes by anabatic winds
208 (Kramer et al., 2010; Xiao et al., 2011). This makes it difficult to use the pollen data to trace past fluctuations in
209 the tree-line and the vegetation composition of the catchment. Fortunately, these studies also indicate that the lake
210 surface pollen spectra from different vegetation types still closely correlate with the environmental gradients
211 (Kramer et al., 2010; Xiao et al., 2011). In addition, theoretical models of pollen transport show that the proportion
212 of the non-local pollen component deposited in lake sediments increases with increasing lake size (Jackson and
213 Lyford, 1999; Sugita, 1994). Thus, the pollen assemblages from Wuxu Lake, which is relatively small, should
214 reliably reflect the response of the regional vegetation composition to changes in climate. The inferred changes in
215 vegetation and climate are summarized below.

216 The pollen spectra between 12.3 and 11.3 cal ka BP are characterized by high percentages of Gramineae,
217 Cyperaceae, *Artemisia*, *Polygonum*, *Thalictrum* and Ranunculaceae, with relatively high percentages of *Salix*,
218 *Hippophae* and Ericaceae. The high shrub and herbaceous pollen percentages indicate the expansion of alpine
219 shrubs and meadows and open vegetation cover around Wuxu Lake, reflecting weak summer rainfall during the

220 late Younger Dryas (YD). The gradually decreasing herbaceous representation also indicates that the ISM had
221 begun to strengthen. During this period, the surrounding arboreal vegetation was dominated by broadleaved
222 deciduous forest, together with *Picea/Abies* forest and sclerophyllous *Quercus*. The dominance of cold-tolerant
223 species in the forest vegetation suggests lower winter temperatures and gradually increasing precipitation in
224 summer.

225 From 11.3 to 10.4 cal ka BP, the decreases in herbaceous pollen, *Salix* and Ericaceae, and significant
226 increases in *Betula*, reflect the replacement of shrubland and meadow by *Betula* woodland. *Pinus*, *Picea/Abies*,
227 *Carpinus*, deciduous and sclerophyllous *Quercus* were common. These changes indicate that the vegetation around
228 Wuxu Lake gradually became closed and that the climate became more seasonal, with warmer and wetter summers
229 and cold winters.

230 The gradual decrease of *Betula* and *Carpinus*, and the slight increase of *Tsuga*, Actinidiaceae, *Rubus*,
231 Rosaceae, *Potentilla*, Gesneriaceae, Labiatae and *Hypericum* until 8.2 cal ka BP, indicate that the vegetation cover
232 was closed. The deciduous broadleaved forest began to retreat and conifer and broadleaved mixed forest with
233 *Tsuga* appeared within the vertical vegetation belts. Actinidiaceae and *Rubus* replaced *Salix* and Ericaceae, forming
234 the understory. These vegetation changes indicate that the climate was very humid in summer and gradually
235 became warmer in winter.

236 From 8.2 to 6.6 cal ka BP. The continuous increase of *Tsuga* and sclerophyllous *Quercus*, and the gradual
237 decrease of *Betula* and *Picea/Abies* between 8.2 and 6.6 cal ka BP, suggest that mixed forest continued to expand
238 towards Wuxu Lake. These vegetation changes indicate that the summers were rather dry and that there was
239 reduced seasonality of temperature.

240 From 6.6 to 4.9 cal ka BP, the relatively high representation of sclerophyllous *Quercus*, increased
241 Actinidiaceae and *Rubus* and steadily decreasing *Betula* and *Picea/Abies* suggest the presence of sclerophyllous
242 *Quercus* forest with a dense understory gradually replacing deciduous broadleaved forest and *Picea/Abies* forest.
243 The summers were humid and the winters were warm.

244 Since 4.9 cal ka BP, the significantly high representation of herbaceous pollen taxa (including *Artemisia*,
245 Gramineae and Cyperaceae), *Hippophae* and Ericaceae indicates that the regional vegetation cover became more
246 open compared to the early Holocene. Increased sclerophyllous *Quercus*, *Tsuga* and decreased *Betula* suggest an
247 expansion of *Tsuga* forest, accompanied by the retreat of *Betula* forest and a slight expansion of *Carpinus* forest.

248 The summers were relatively dry and the winters warmer, compared to the preceding interval.

249 After 2.6 cal ka BP, *Betula* forest was further replaced by sclerophyllous *Quercus*. *Tsuga* and *Alnus* remained
250 at a similar level as during the preceding stage. The slight decrease in *Artemisia*, Cyperaceae, Gramineae and
251 Ranunculaceae indicates that the alpine meadows retreated, while increase in Rosaceae, *Potentilla*, Gesneriaceae,
252 Labiatae and *Hypericum* suggests that the forest was relatively closed. With humid summers and warm winters the
253 climate was more favorable compared to the preceding interval. The minor increase in *Sanguisorba*, a grazing
254 indicator (Kramer et al., 2010), suggests the influence of human activity in the region.

255

256

257

258 **5.2 Timing of the Holocene**

259 The YD is the last millennial-scale cooling event before the beginning of the Holocene in the Northern
260 Hemisphere (Stuiver et al., 1995). In the ISM region, a roughly contemporaneous cold and dry event has been
261 observed in numerous records but in general they are of low resolution. At about 11.3 cal ka BP, the abrupt
262 decrease of PCA 2 axis sample scores may reflect the termination of the YD cold event in the region. A high
263 resolution stalagmite $\delta^{18}\text{O}$ record from Moomi Cave in Yemen exhibits a sharp fall at about 11.4 ka BP, marking
264 the onset of the Holocene (Shakun et al., 2007). A pollen and stoma record from Tiancai Lake in southwestern
265 China also suggests that the age of the termination of the YD was about 11.5 cal ka BP (Xiao et al., 2014a).
266 However, other records, such as pollen records from Erhai Lake and Naleng Lake (Kramer et al., 2010; Shen et al.,
267 2006), and stable carbon isotope record from Muge Co (Sun et al., 2015) show relative large uncertainties due to
268 the bulk sediment dated. Thus the timings in the ISM region are generally consistent with the age of the YD
269 termination in the Greenland ice core record (Stuiver et al., 1995).

270 Several factors may be responsible for the 200-year time lag in the Wuxu Lake record. Firstly, the stage for
271 vegetation succession: e.g., the *Abies/Picea* form the climax forest in the subalpine ecotone after glacier retreat in
272 northwestern Sichuan took about 100 years (Cheng and Luo, 2004). Pollen records from North America and
273 Europe also show that vegetation may lag climate change by 100-200 years (Williams et al., 2002). Secondly,
274 the influence of centennial scale event may have hindered our pollen record to distinguish the short event as the

275 YD (Rasmussen, 2006; Shakun et al., 2007). Thirdly, errors in the AMS ^{14}C dates could also be responsible for the
276 200-year time lag (the 95% confidence limit of the point ranges from 11.0 to 11.6 cal ka BP).

277 **5.3 Structure of the Holocene climatic optimum**

278 The onset of warm and humid conditions around Wuxu Lake occurred after 10.4 cal ka BP and was
279 maintained until 4.9 cal ka BP, resulting in a prolonged Holocene Optimum except for a relative cold pulse
280 between 8.2 and 6.6 cal ka BP. (Fig. 6a). The $\delta^{18}\text{O}$ and δD values of rainfall reflect changes in isotopic
281 composition in moisture source areas and by transport distance, and are not correlated with seasonal rainfall
282 amount. However, in the ISM region these isotope ratios are suggested to reflect monsoon intensity over time
283 spans longer than the annual scale (Breitenbach et al., 2010; Contreras-Rosales et al., 2014). High resolution
284 stalagmite $\delta^{18}\text{O}$ records from Qunf Cave in southern Oman (Fig. 6b) and Tianmen Cave in southern QTP (Fig. 6e)
285 indicate an interval of strong ISM in the early Holocene, followed by a progressive weakening trend at about 6-7
286 ka BP (Cai et al., 2012; Fleitmann et al., 2003). Records of carbonate $\delta^{18}\text{O}$ and plant wax δD from lake and marine
287 sediments, which reflect the isotopic composition of the precipitation, reveal a similar trend (Fig. 6d, Bird et al.,
288 2014; Contreras-Rosales et al., 2014; Sarkar et al., 2015). Thus, the traditional view suggests that a warm and
289 humid climate with a strong summer monsoon occurred during the first half of the Holocene in the ISM region
290 (Fig. 6f, Wang et al., 2010; Zhang et al., 2011), coinciding with gradual changes in northern Hemisphere summer
291 insolation (Fig. 6c, Berger and Loutre, 1991). The abrupt monsoonal intensification and the early- to-
292 mid-Holocene climatic optimum around Wuxu Lake are in accord with this view. In detail, the climatic optimum
293 exhibits two peaks, at 10.4-8.2 cal ka BP and 6.6-4.9 cal ka BP, with a slight reduction between 8.2 and 6.6 cal ka
294 BP. However, in the ISM region only the early stage of the Holocene monsoonal maximum is well documented in
295 paleoclimatic records with reliable age control. In the Hajar Mountain range in northern Oman, sediment
296 accumulation rates based on optically stimulated luminescence dating show that the early Holocene humid period
297 began at 10.5 ka BP, and reached a maximum at 9.0–8.0 ka BP (Fuchs and Buerkert, 2008). Sedimentation data
298 from Paru Co from the southern QTP suggest that the ISM precipitation maximum occurred during the early
299 Holocene, between 10.1 and 7.1 cal ka BP (Fig. 6h, Bird et al., 2014). In addition, reconstructed monsoon
300 precipitation based on pollen assemblages from Xingyun Lake in southwest China reached a maximum during the
301 interval 7.8-7.5 cal ka BP (Fig. 6g, Chen et al., 2014). This general pattern of the Holocene climatic optimum is
302 also observed in several other records from the QTP, but are affected by the carbon reservoir effect. A pollen
303 record from Tso Kar in northwestern India indicates a rapid increase in summer monsoon precipitation from 10.8

304 to 9.2 cal ka BP, a moderate reduction in precipitation between 9.2 and 6.8 cal ka BP, and a second precipitation
305 pulse from 6.9 and 4.8 cal ka BP (Fig. 6i, Demske et al., 2009). Similarly, the record from Lake Naleng in the
306 southeastern QTP indicates relatively stable, warm and humid conditions from 10.7 to 4.4 cal ka BP, except for the
307 interval between 8.1 and 7.2 cal ka BP (Fig. 6j, Kramer et al., 2010). In addition, reconstructed total solar
308 irradiance based on cosmogenic radionuclides indicates significantly weakened solar activity between 8 and 7 ka
309 BP (Steinhilber et al., 2012). Furthermore, a ~90-year periodicity in the pollen record from Wuxu Lake has also
310 been documented in the stalagmite $\delta^{18}\text{O}$ record from Qunf Cave in southern Oman (Fleitmann et al., 2003), and is
311 close to the significant 87-year periodicity of the $\Delta^{14}\text{C}$ record (Stuiver and Braziunas, 1993). This correspondence
312 suggests a link between solar irradiance and ISM variability during the Holocene.

313 Most of the records from the QTP indicate that the climate became cold and dry in the late Holocene,
314 suggesting that the environment of the QTP and the adjacent region was predominantly influenced by the ISM
315 (Sun et al., 2015). However, the inconsistency in the timing and duration of the Holocene climatic optimum
316 indicates the occurrence of local variations in rainfall amount in response to the ISM (Bird et al., 2014), which is
317 compatible with the complex terrain of the margin of the QTP. The topography effect of the Tibetan Plateau affects
318 the moisture transfer path and establishes unstable potential energy stratification (Chen et al., 2007; Houze, 2012).
319 The steep terrain of the margin of the QTP strengthens ascending air motions, promoting the release of latent heat
320 and the rapid development of strong convection. Because of their high elevations, the mountains block low level
321 airflows to the windward sides and significantly reduce moisture transport to the interior. Until now, the long
322 duration of the Holocene climatic optimum has only been observed in records from the margin of the QTP,
323 suggesting that local topography and rain-shadow effects may also have played an important role in the Holocene
324 moisture evolution of the QTP.

325 **5.4 Relationship between the Wuxu Lake paleovegetation record and the EAWM**

326 It was suggested above that the first PCA axis may reflect winter temperature. Since the winter temperature
327 in China is negatively correlated with the intensity of the EAWM (Guo, 1994; Ren, 1990), it can be assumed that
328 the sample scores on PCA axis 1 are a proxy for the EAWM intensity. The record from Wuxu Lake suggests that
329 the EAWM was strong from the late YD to the early Holocene, and that it gradually weakened in the late Holocene
330 (Fig. 7a). The overall trend of the EAWM during the past 12.3 ka probably followed gradual changes in Northern
331 Hemisphere winter insolation (Fig. 7b, Berger and Loutre, 1991). A strong EAWM in the early Holocene is
332 consistent with other records from the Chinese monsoonal region. For example, the diatom record from

333 Huguangyan Lake in southern China indicates that the water column was well mixed in the early Holocene, mainly
334 as the result of cold, windy conditions during winter (Fig. 7c, Wang et al., 2012). This hypothesis is further
335 supported by the records of total organic carbon content and $\delta^{15}\text{N}$ from the same lake (Jia et al., 2015). The larger
336 sea surface temperature (SST) gradients over the South China Sea reveal a strengthened EAWM during the early
337 Holocene (Fig. 7d to 7f, Huang et al., 2011; Steinke et al., 2011; Steinke et al., 2010). However, the grain-size
338 record of Chinese loess deposits also indicates that the EAWM winds gradually weakened from the early Holocene
339 to the mid Holocene, and then gradually strengthened in the late Holocene (Fig. 7g, Sun et al., 2012), a similar
340 pattern to that recorded by geochemical parameters from Gonghe Basin in the northeastern QTP (Liu et al., 2013).
341 The discrepancies may be due to the fact that the grain-size of loess and dune mobility were also influenced by the
342 advance or retreat of deserts in northern China (Mason et al., 2008; Yang and Ding, 2008).

343 Interestingly, the pollen record from Wuxu Lake suggests that the EAWM was weaker in the late YD than in
344 the early Holocene. However, this finding is in conflict with the diatom record from Huguangyan Lake, which
345 indicates that the EAWM intensified significantly in response to abrupt climate change in the North Atlantic Ocean
346 (Fig. 7c, Wang et al., 2012). The records from the South China Sea also indicate an intensified EAWM during this
347 interval, in response to the slowdown of the Atlantic meridional overturning circulation (Fig. 7d to 7f, Huang et al.,
348 2011; Steinke et al., 2011; Steinke et al., 2010). However, it should be noted that the marine records are poorly
349 dated and are of low temporal resolution. The anomaly may be explained by the climate in the tropical eastern
350 Pacific. Observation data show that a strong EAWM usually occurs when there is a negative SST anomaly in the
351 tropical eastern Pacific (La Niña), while a positive anomaly (El Niño) is usually accompanied by a weak EAWM
352 (Chen et al., 2000; Wang et al., 2000). A model study indicates a significant enhancement of the El Niño Southern
353 Oscillation (ENSO) amplitude during the YD (Liu et al., 2014), which accords with the weak EAWM revealed by
354 the Wuxu Lake record (Fig. 7h). Furthermore, a gradual intensification of ENSO during the Holocene also accords
355 with a weakened EAWM, ~~suggesting that low latitude climate processes also played an important role in the~~
356 ~~EAWM evolution during the past 12.3 ka.~~

357 **5.5 Relationship between the EAWM and ISM**

358 Previous studies of the dust deposits of the Chinese Loess Plateau indicate that the winter monsoon is
359 negatively correlated with the summer monsoon on orbital and millennial time scales (Porter, 2001; Sun et al.,
360 2012). As mentioned above, the grain-size of loess is controlled by both the winter wind intensity and the summer
361 precipitation. Comparison of the EAWM proxy record (Fig. 8a) with the stalagmite $\delta^{18}\text{O}$ record from Qunf Cave in

362 southern Oman (Fig. 8c, Fleitmann et al., 2003) and with the plant wax δD record from the northern Bay of Bengal
363 (Fig. 8d, Contreras-Rosales et al., 2014), which are ISM intensity records, reveals a broadly in-phase relationship
364 between the EAWM and ISM in the past 12.3 ka and suggests a stronger seasonal contrast during the early
365 Holocene than during the late Holocene. This stronger seasonal contrast during the early Holocene clearly tracks
366 solar insolation differences between the winter and summer seasons (Fig. 8b and e, Berger and Loutre, 1991).
367 During the Holocene, increases in winter insolation and in winter temperature at high latitudes of the Northern
368 Hemisphere reduced the intensity of the Siberian High and resulted in a weak EAWM; however, decreased
369 summer insolation caused the southward migration of the intertropical convergence zone and resulted in a weak
370 ISM (Wang et al., 2012). In addition, solar insolation in the Southern Hemisphere was relatively low and El Niño
371 strength was relatively weak during the early Holocene (Fig. 8e and f, Berger and Loutre, 1991; Liu et al., 2014),
372 which would probably have promoted both a strong EAWM and ISM (Chen et al., 2000; Kumar et al., 1999; Wang
373 et al., 2000). Based on historical documents from eastern China, a relationship between the frequency of cold
374 winters and summer rainfall during AD 700-900 further supports the notion that the strength of the winter
375 monsoon is in-phase with the summer monsoon (Zhang and Lu, 2007).

376

377 **6. Conclusions**

378 We have reconstructed variations in the EAWM and ISM during the late deglaciation and the Holocene based
379 on a well-dated pollen record from Wuxu Lake in southwestern China. Our findings are generally consistent with
380 previous studies: The EAWM was strong in the early Holocene and weakened in the late Holocene. However, in
381 contrast to other studies, our results suggest that the EAWM was slightly weaker during the YD event than in the
382 early Holocene. Our record indicates that the ISM began to strengthen at about 11.3 cal ka BP, corresponding to
383 the termination of the YD in the Northern Hemisphere. The Holocene climatic optimum, in terms of maximum
384 precipitation, persisted from 10.4 to 4.9 cal ka BP, and we attribute this long duration on the margin of the QTP to
385 the complex topography of the area and related orographic effects. This inconsistency in the onset and duration of
386 the strengthened ISM may reflect a discrepancy in local rainfall response to the ISM. Overall, the EAWM is
387 broadly in-phase with the ISM, both of which decrease in strength from the early to the late Holocene, which is
388 caused by the interplay of solar insolation between the winter and summer seasons and ENSO strength in the
389 tropical Pacific.

390

391 **Acknowledgements**

392 We thank two anonymous reviewers who gave us important advice which improved the quality of the
393 manuscript. We also thank Jan Bloemendal for correcting the English language, and Q. Jiang, H. Tang for field
394 assistance. This project was supported by the Strategic Priority Research Program–Climate Change: Carbon Budget
395 and Relevant Issues of the Chinese Academy of Sciences (Grant no. XDA05120102) and NIGLAS (2012135004),
396 and the National Natural Science Foundation of China (no. 41272380).

397 **References**

- 398 An, Z., Porter, S. C., Kutzbach, J. E., Wu, X., Liu, X., Li, X., and Zhou, W.: Asynchronous Holocene
399 optimum of the East Asian monsoon, *Quaternary Sci. Rev.*, 19, 743–762, 2000.
- 400 An, Z., Clemens, S. C., Shen, J., Qiang, X., Jin, Z., Sun, Y., Prell, W. L., Luo, J., Wang, S., Xu, H., Cai,
401 Y., Zhou, W., Liu, X., Liu, W., Shi, Z., Yan, L., Xiao, X., Chang, H., Wu, F., Ai, L., and Lu, F.:
402 Glacial–interglacial Indian Summer monsoon dynamics, *Science*, 333, 719–723, 2011.
- 403 Berger, A. and Loutre, M.-F.: Insolation values for the climate of the last 10 million years, *Quaternary*
404 *Sci. Rev.*, 10, 297–317, 1991.
- 405 Bird, B. W., Polisar, P. J., Lei, Y., Thompson, L. G., Yao, T., Finney, B. P., Bain, D. J., Pompeani, D. P.,
406 and Steinman, B. A.: A Tibetan lake sediment record of Holocene Indian summer monsoon variability,
407 *Earth Planet. Sc. Lett.*, 399, 92–102, 2014.
- 408 Blaauw, M., Andres Christen, J.: Flexible paleoclimate age-depth models using an autoregressive
409 gamma process, *Bayesian Analysis*, 6, 457–474, 2011.
- 410 Breitenbach, S. F. M., Adkins, J. F., Meyer, H., Marwan, N., Kumar, K. K., and Haug, G. H.: Strong
411 influence of water vapor source dynamics on stable isotopes in precipitation observed in Southern
412 Meghalaya, NE India, *Earth Planet. Sc. Lett.*, 292, 212–220, 2010.
- 413 Cai, Y., Zhang, H., Cheng, H., An, Z., Lawrence Edwards, R., Wang, X., Tan, L., Liang, F., Wang, J.,
414 and Kelly, M.: The Holocene Indian monsoon variability over the southern Tibetan Plateau and its
415 teleconnections, *Earth Planet. Sc. Lett.*, 335–336, 135–144, 2012.
- 416 Chen, F., Chen, X., Chen, J., Zhou, A., Wu, D., Tang, L., Zhang, X., Huang, X., and Yu, J.: Holocene
417 vegetation history, precipitation changes and Indian Summer Monsoon evolution documented from
418 sediments of Xingyun Lake, south-west China, *J. Quaternary Sci.*, 29, 661–674, 2014.
- 419 Chen, J., Li, C., and He, G.: A diagnostic analysis of the impact of complex terrain in the eastern
420 Tibetan Plateau, China, on a severe storm, *Arct. Antarct. Alp. Res.*, 39, 699–707, 2007.
- 421 Chen, W., Graf, H.-F., and Huang, R.: The interannual variability of East Asian Winter Monsoon and its
422 relation to the summer monsoon, *Adv. Atmos. Sci.*, 17, 48–60, 2000.
- 423 Cheng, G. and Luo, J.: Succession features and dynamic simulation of subalpine forest in the Gongga
424 Mountain, China, *J. Mt. Sci.*, 1, 29–37, 2004.
- 425 Cheng, H., Edwards, R. L., Ho, J., Gallup, C. D., Richards, D. A., and Asmerom, Y.: The halflives of
426 uranium-234 and thorium-230, *Chem. Geol.*, 169, 17–33, 2000.
- 427 Contreras-Rosales, L. A., Jennerjahn, T., Tharammal, T., Meyer, V., Lückge, A., Paul, A., and Schefuß
428 E.: Evolution of the Indian Summer Monsoon and terrestrial vegetation in the Bengal region during the

429 past 18 ka, *Quaternary Sci. Rev.*, 102, 133–148, 2014.

430 Cook, C. G., Jones, R. T., and Turney, C. S. M.: Catchment instability and Asian summer monsoon
431 variability during the early Holocene in southwestern China, *Boreas*, 42, 224–235, 2013.

432 Demske, D., Tarasov, P. E., Wünnemann, B., and Riedel, F.: Late glacial and Holocene vegetation,
433 Indian monsoon and westerly circulation in the Trans-Himalaya recorded in the lacustrine pollen
434 sequence from Tso Kar, Ladakh, NW India, *Palaeogeogr. Palaeoclimatol.*, 279, 172–185, 2009.

435 Fægri, K., Kaland, P. E., and Krzywinski, K.: *Textbook of Pollen Analysis*, 4th edn., John Wiley and
436 Sons, Chichester, 1989.

437 Fleitmann, D., Burns, S. J., Mudelsee, M., Neff, U., Kramers, J., Mangini, A., and Matter, A.: Holocene
438 forcing of the Indian monsoon recorded in a stalagmite from southern Oman, *Science*, 300, 1737–1739,
439 2003.

440 Fleitmann, D., Burns, S. J., Mangini, A., Mudelsee, M., Kramers, J., Villa, I., Neff, U., Al-Subbary, A.
441 A., Buettner, A., Hippler, D., and Matter, A.: Holocene ITCZ and Indian monsoon dynamics recorded
442 in stalagmites from Oman and Yemen (Socotra), *Quaternary Sci. Rev.*, 26, 170–188, 2007.

443 Fuchs, M. and Buerkert, A.: A 20 ka sediment record from the Hajar Mountain range in N-Oman, and
444 its implication for detecting arid–humid periods on the southeastern Arabian Peninsula, *Earth Planet.
445 Sc. Lett.*, 265, 546–558, 2008.

446 Grimm, E. C.: CONISS: a FORTRAN 77 program for stratigraphically constrained cluster analysis by
447 the method of incremental sum of squares, *Comput. Geosci.*, 13, 13–35, 1987.

448 Guo, Q.: Relationship between the variations of East Asian winter monsoon and temperature anomalies
449 in China, *Quarterly J. Appl. Meteorol.*, 5, 218–225, 1994 (in Chinese).

450 Gupta, A. K., Anderson, D. M., and Overpeck, J. T.: Abrupt changes in the Asian southwest monsoon
451 during the Holocene and their links to the North Atlantic Ocean, *Nature*, 421, 354–357, 2003.

452 Hou, J., D’Andrea, W. J., and Liu, Z.: The influence of ^{14}C reservoir age on interpretation of
453 paleolimnological records from the Tibetan Plateau, *Quaternary Sci. Rev.*, 48, 67–79, 2012.

454 Houze, R. A.: Orographic effects on precipitating clouds, *Rev. Geophys.*, 50, RG1001,
455 doi:10.1029/2011RG000365, 2012.

456 Huang, E., Tian, J., and Steinke, S.: Millennial-scale dynamics of the winter cold tongue in the
457 southern South China Sea over the past 26 ka and the East Asian winter monsoon, *Quaternary Res.*, 75,
458 196–204, 2011.

459 Jackson, S. and Lyford, M.: Pollen dispersal models in Quaternary plant ecology: assumptions,
460 parameters, and prescriptions, *Bot. Rev.*, 65, 39–75, 1999.

461 Jarvis, D. I.: Pollen Evidence of Changing Holocene Monsoon Climate in Sichuan Province, China,
462 *Quaternary Res.*, 39, 325–337, 1993.

463 Jia, G., Bai, Y., Yang, X., Xie, L., Wei, G., Ouyang, T., Chu, G., Liu, Z., and Peng, P. A.:
464 Biogeochemical evidence of Holocene East Asian summer and winter monsoon variability from a
465 tropical maar lake in southern China, *Quaternary Sci. Rev.*, 111, 51–61, 2015.

466 Kramer, A., Herzschuh, U., Mischke, S., and Zhang, C.: Holocene treeline shifts and monsoon
467 variability in the Hengduan Mountains (southeastern Tibetan Plateau), implications from palynological
468 investigations, *Palaeogeogr. Palaeoclimatol.*, 286, 23–41, 2010.

469 Kumar, K. K., Kleeman, R., Cane, M. A., and Rajagopalan, B.: Epochal changes in Indian
470 Monsoon-ENSO precursors, *Geophys. Res. Lett.*, 26, 75–78, 1999.

471 Li, J., Xu, Q., Zheng, Z., Lu, H., Luo, Y., Li, Y., Li, C., and Seppä, H.: Assessing the importance of
472 climate variables for the spatial distribution of modern pollen data in China, *Quaternary Res.*, 83,

473 287–297, 2015.

474 Liu, B., Jin, H., Sun, L., Sun, Z., and Su, Z.: Winter and summer monsoonal evolution in north eastern
475 Qinghai-Tibetan Plateau during the Holocene period, *Chem. Erde-Geochem.*, 73, 309–321, 2013.

476 Liu, Z., Lu, Z., Wen, X., Otto-Bliesner, B. L., Timmermann, A., and Cobb, K. M.: Evolution and
477 forcing mechanisms of El Niño over the past 21,000 years, *Nature*, 515, 550–553, 2014.

478 Maher, B. A.: Holocene variability of the East Asian summer monsoon from Chinese cave records: a
479 re-assessment, *The Holocene*, 18, 861–866, 2008.

480 Maher, B. A. and Thompson, R.: Oxygen isotopes from Chinese caves: records not of monsoon rainfall
481 but of circulation regime, *J. Quaternary Sci.*, 27, 615–624, 2012.

482 Mason, J. A., Swinehart, J. B., Lu, H., Miao, X., Cha, P., and Zhou, Y.: Limited change in dune
483 mobility in response to a large decrease in wind power in semi-arid northern China since the 1970s,
484 *Geomorphology*, 102, 351–363, 2008.

485 Pausata, F. S. R., Battisti, D. S., Nisancioglu, K. H., and Bitz, C. M.: Chinese stalagmite $\delta^{18}\text{O}$
486 controlled by changes in the Indian monsoon during a simulated Heinrich event, *Nat. Geosci.*, 4,
487 474–480, 2011.

488 Porter, S. C.: Chinese loess record of monsoon climate during the last glacial–interglacial cycle,
489 *Earth-Sci. Rev.*, 54, 115–128, 2001.

490 Prasad, S., Anoop, A., Riedel, N., Sarkar, S., Menzel, P., Basavaiah, N., Krishnan, R., Fuller, D.,
491 Plessen, B., Gaye, B., Röhl, U., Wilkes, H., Sachse, D., Sawant, R., Wiesner, M. G., and Stebich, M.:
492 Prolonged monsoon droughts and links to Indo-Pacific warm pool: a Holocene record from Lonar Lake,
493 central India, *Earth Planet. Sc. Lett.*, 391, 171–182, 2014.

494 R Development Core Team: R: a Language and Environment for Statistical Computing, R Foundation
495 for Statistical Computing, Vienna, Austria, 2013.

496 Rashid, H., Flower, B. P., Poore, R. Z., and Quinn, T. M.: A ~25 ka Indian Ocean monsoon variability
497 record from the Andaman Sea, *Quaternary Sci. Rev.*, 26, 2586–2597, 2007.

498 Rasmussen, S. O., Andersen, K. K., Svensson, A. M., Steensen, J. P., Vinther, B. M., Clausen, H. B.,
499 Andersen, M. L., Johnsen, S. J., Larsen, L. B., Bigler, M., Röhlisberger,
500 R., Fischer, H., Goto-Azuma, K., Hansson, M. E., and Ruth, U.: A new Greenland ice core chronology
501 for the last glacial termination, *J. Geophys. Res.-Atmos.*, 111, D06102, doi:10.1029/2005JD006079,
502 2006.

503 Reimer, P. J., Bard, E., Bayliss, A., Beck, J. W., Blackwell, P. G., Ramsey, C. B., Buck, C. E., Cheng, H.,
504 Edwards, R. L., and Friedrich, M.: IntCal13 and Marine13 radiocarbon age calibration curves 0–50,000
505 years cal BP, *Radiocarbon*, 55, 1869–1887, 2013.

506 Ren, G.: Winter monsoon and air temperature over East Asia region, *Sci. Geogr. Sin.*, 10, 257–263,
507 1990 (in Chinese).

508 Sarkar, S., Prasad, S., Wilkes, H., Riedel, N., Stebich, M., Basavaiah, N., and Sachse, D.: Monsoon
509 source shifts during the drying mid-Holocene: biomarker isotope based evidence from the core
510 “monsoon zone” (CMZ) of India, *Quaternary Sci. Rev.*, 123, 144–157, 2015.

511 Schulz M. and Mudelsee M.: REDFIT: estimating red-noise spectra directly from unevenly spaced
512 paleoclimatic time series. *Computers & Geosciences* 28, 421–426, 2002.

513 Shakun, J. D., Burns, S. J., Fleitmann, D., Kramers, J., Matter, A., and Al-Subary, A.: A highresolution,
514 absolute-dated deglacial speleothem record of Indian Ocean climate from Socotra Island, Yemen, *Earth
515 Planet. Sc. Lett.*, 259, 442–456, 2007.

516 Shen, C., Liu, K.-b., Tang, L., and Overpeck, J. T.: Quantitative relationships between modern pollen

517 rain and climate in the Tibetan Plateau, *Rev. Palaeobot. Palyno.*, 140, 61–77, 2006.

518 Shen, J., Liu, X., Wang, S., and Ryo, M.: Palaeoclimatic changes in the Qinghai Lake area during the
519 last 18,000 years, *Quaternary Int.*, 136, 131–140, 2005.

520 Shen, J., Jones, R. T., Yang, X., Dearing, J. A., and Wang, S.: The Holocene vegetation history of Lake
521 Erhai, Yunnan province southwestern China: the role of climate and human forcings, *The Holocene*, 16,
522 265–276, 2006.

523 Shen, J., Wu, X., Zhang, Z., Gong, W., He, T., Xu, X., and Dong, H.: Ti content in Huguangyan maar
524 lake sediment as a proxy for monsoon-induced vegetation density in the Holocene, *Geophys. Res. Lett.*,
525 40, 5757–5763, 2013.

526 Song, X.-Y., Yao, Y.-F., Wortley, A. H., Paudyal, K. N., Yang, S.-H., Li, C.-S., and Blackmore, S.:
527 Holocene vegetation and climate history at Haligu on the Jade Dragon Snow Mountain, Yunnan, SW
528 China, *Climatic Change*, 113, 841–866, 2012.

529 Steinhilber, F., Abreu, J. A., Beer, J., Brunner, I., Christl, M., Fischer, H., Heikkilä U., Kubik, P.W.,
530 Mann, M., and McCracken, K. G.: 9,400 years of cosmic radiation and solar activity from ice cores and
531 tree rings, *P. Natl. Acad. Sci. USA*, 109, 5967–5971, 2012.

532 Steinke, S., Mohtadi, M., Groeneveld, J., Lin, L.-C., Löwemark, L., Chen, M.-T., and Rendle-Bühning,
533 R.: Reconstructing the southern South China Sea upper water column structure since the Last Glacial
534 Maximum: implications for the East Asian winter monsoon development, *Paleoceanography*, 25,
535 PA2219, doi:10.1029/2009PA001850, 2010.

536 Steinke, S., Glatz, C., Mohtadi, M., Groeneveld, J., Li, Q., and Jian, Z.: Past dynamics of the East
537 Asian monsoon: no inverse behaviour between the summer and winter monsoon during the Holocene,
538 *Global Planet. Change*, 78, 170–177, 2011.

539 Stevens, T., Thomas, D. S. G., Armitage, S. J., Lunn, H. R., and Lu, H.: Reinterpreting climate proxy
540 records from late Quaternary Chinese loess: a detailed OSL investigation, *Earth-Sci. Rev.*, 80, 111–136,
541 2007.

542 Stuiver, M. and Braziunas, T. F.: Sun, ocean, climate and atmospheric $^{14}\text{CO}_2$: an evaluation of causal
543 and spectral relationships, *The Holocene*, 3, 289–305, 1993.

544 Stuiver, M., Grootes, P. M., and Braziunas, T. F.: The GISP2 $\delta^{18}\text{O}$ climate record of the past 16,500
545 years and the role of the sun, ocean, and volcanoes, *Quaternary Res.*, 44, 341–354, 1995.

546 Sugita, S.: Pollen representation of vegetation in quaternary sediments: theory and method in patchy
547 vegetation, *J. Ecol.*, 82, 881–897, 1994.

548 Sun, W., Zhang, E., Jones, R. T., Liu, E., and Shen, J.: Asian summer monsoon variability during
549 the late glacial and Holocene inferred from the stable carbon isotope record of black carbon in the
550 sediments of Muge Co, southeastern Tibetan Plateau, China, *The Holocene*, 25, 1857–1868, 2015.

551 Sun, Y., Clemens, S. C., Morrill, C., Lin, X., Wang, X., and An, Z.: Influence of Atlantic meridional
552 overturning circulation on the East Asian winter monsoon, *Nat. Geosci.*, 5, 46–49, 2012.

553 Tan, M.: Circulation effect: response of precipitation $\delta^{18}\text{O}$ to the ENSO cycle in monsoon regions of
554 China, *Clim. Dynam.*, 42, 1067–1077, 2014.

555 ter Braak, C. J. F. and Milauer, P.: CANOCO Reference Manual and Cano-Draw for Windows User's
556 Guide: Software for Canonical Community Ordination (Version, 4.5), Microcomputer Power, Ithaca,
557 2002.

558 Tian, J., Huang, E., and Pak, D. K.: East Asian winter monsoon variability over the last glacial cycle:
559 insights from a latitudinal sea-surface temperature gradient across the South China Sea, *Palaeogeogr.*
560 *Palaeocl.*, 292, 319–324, 2010.

561 Wang, B., Wu, R., and Fu, X.: Pacific–East Asian teleconnection: how does ENSO affect East Asian
562 climate?, *J. Climate*, 13, 1517–1536, 2000.

563 Wang, L., Li, J., Lu, H., Gu, Z., Rioual, P., Hao, Q., Mackay, A. W., Jiang, W., Cai, B., Xu, B., Han, J.,
564 and Chu, G.: The East Asian winter monsoon over the last 15,000 years: its links to high-latitudes and
565 tropical climate systems and complex correlation to the summer monsoon, *Quaternary Sci. Rev.*, 32,
566 131–142, 2012.

567 Wang, Y., Liu, X., and Herzschuh, U.: Asynchronous evolution of the Indian and East Asian Summer
568 Monsoon indicated by Holocene moisture patterns in monsoonal central Asia, *Earth-Sci. Rev.*, 103,
569 135–153, 2010.

570 Wang, Y. J., Cheng, H., Edwards, R. L., An, Z. S., Wu, J. Y., Shen, C.-C., and Dorale, J. A.: A
571 high-resolution absolute-dated late Pleistocene monsoon record from Hulu Cave, China, *Science*, 294,
572 2345–2348, 2001.

573 Williams, J. W., Post, D. M., Cwynar, L. C., Lotter, A. F., and Levesque, A. J.: Rapid and widespread
574 vegetation responses to past climate change in the North Atlantic region, *Geology*, 30, 971–974, 2002.

575 Wischniewski, J., Kramer, A., Kong, Z., Mackay, A. W., Simpson, G. L., Mischke, S., and Herzschuh,
576 U.: Terrestrial and aquatic responses to climate change and human impact on the southeastern Tibetan
577 Plateau during the past two centuries, *Glob. Change Biol.*, 17, 3376–3391, 2011.

578 Wu, Z., Hou, X., and Zhu, Y.: *Chinese Vegetation*, Science Press, Beijing, 1980 (in Chinese). Xiao, X.,
579 Shen, J., and Wang, S.: Spatial variation of modern pollen from surface lake sediments in Yunnan and
580 southwestern Sichuan Province, China, *Rev. Palaeobot. Palyno.*, 165, 224–234, 2011.

581 Xiao, X., Haberle, S. G., Shen, J., Yang, X., Han, Y., Zhang, E., and Wang, S.: Latest Pleistocene and
582 Holocene vegetation and climate history inferred from an alpine lacustrine record, northwestern
583 Yunnan Province, southwestern China, *Quaternary Sci. Rev.*, 86, 35–48, 2014a.

584 Xiao, X., Haberle, S. G., Yang, X., Shen, J., Han, Y., and Wang, S.: New evidence on deglacial climatic
585 variability from an alpine lacustrine record in northwestern Yunnan Province, southwestern China,
586 *Palaeogeogr. Palaeoclimatol.*, 406, 9–21, 2014b.

587 Yancheva, G., Nowaczyk, N. R., Mingram, J., Dulski, P., Schettler, G., Negendank, J. F. W., Liu, J.,
588 Sigman, D. M., Peterson, L. C., and Haug, G. H.: Influence of the intertropical convergence zone on the
589 East Asian monsoon, *Nature*, 445, 74–77, 2007.

590 Yang, S. and Ding, Z.: Advance–retreat history of the East-Asian summer monsoon rainfall belt over
591 northern China during the last two glacial–interglacial cycles, *Earth Planet. Sc. Lett.*, 274, 499–510,
592 2008.

593 Yu, G., Tang, L., Yang, X., Ke, X., and Harrison, S. P.: Modern pollen samples from alpine vegetation
594 on the Tibetan Plateau, *Global Ecol. Biogeogr.*, 10, 503–519, 2001.

595 Zhang, D. E. and Lu, L.: Anti-correlation of summer/winter monsoons?, *Nature*, 450, E7–E8, 2007.

596 Zhang, J., Chen, F., Holmes, J. A., Li, H., Guo, X., Wang, J., Li, S., Lü Y., Zhao, Y., and Qiang, M.:
597 Holocene monsoon climate documented by oxygen and carbon isotopes from lake sediments and peat
598 bogs in China: a review and synthesis, *Quaternary Sci. Rev.*, 30, 1973–1987, 2011.

599 Zhou, H., Wang, B.-S., Guan, H., Lai, Y.-J., You, C.-F., Wang, J., and Yang, H.-J.: Constraints from
600 strontium and neodymium isotopic ratios and trace elements on the sources of the sediments in Lake
601 Huguang Maar, *Quaternary Res.*, 72, 289–300, 2009.

602

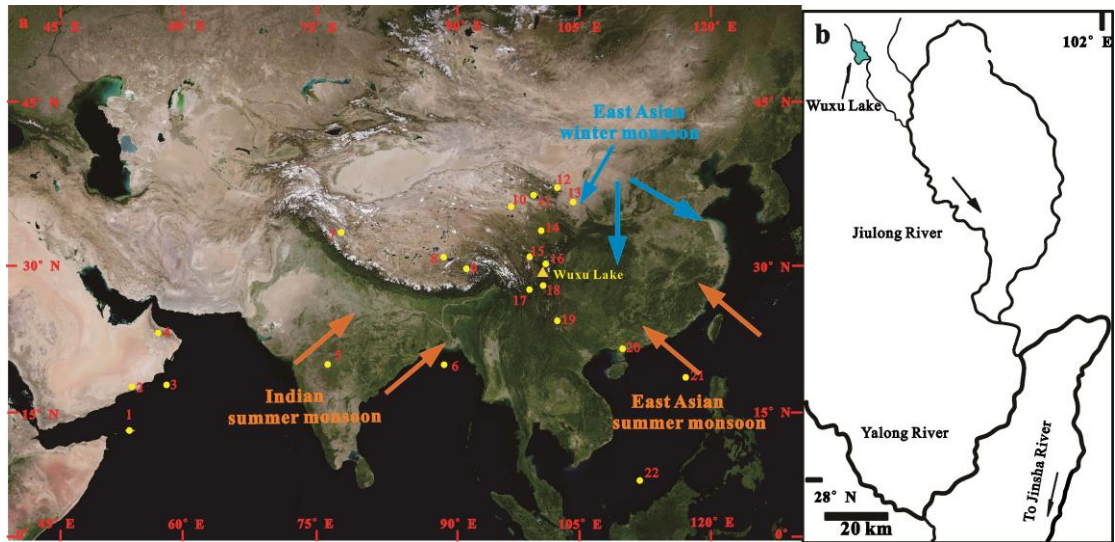
603

604

605 **Table 1.** AMS radiocarbon dates of terrestrial plant from Wuxu Lake. All of the AMS ^{14}C dates are
606 calibrated to calendar years before present using the IntCal13 calibration dataset (Reimer et al., 2013).

Lab number	sample depth (cm)	Material dated	^{14}C ages (yr BP)	cal year BP (2σ)	Median age (cal yr BP)
NZA35824	76	Plant remains	306 \pm 20	303-452	393
NZA35825	114	Plant remains	785 \pm 20	679-730	704
NZA 35827	212	Plant remains	1979 \pm 20	1883-1987	1926
Beta 306665	296	Plant remains	2230 \pm 30	2153-2333	2228
Beta 306666	410	Plant remains	3510 \pm 30	3698-3865	3777
Beta 306667	478	Plant remains	4150 \pm 30	4577-4825	4695
NZA 35832	557	Plant remains	4500 \pm 25	5047-5293	5167
Beta 306668	616	Plant remains	4790 \pm 30	5470-5593	5517
Beta 306669	672	Plant remains	5420 \pm 40	6031-6300	6235
Beta 306670	732	Plant remains	5980 \pm 40	6721-6936	6819
Beta 306671	819	Plant remains	7240 \pm 40	7978-8162	8059
Beta 306672	862	Plant remains	7870 \pm 50	8547-8975	8680
Beta 306673	904	Plant remains	8110 \pm 40	8983-9242	9052
Beta 306674	920	Plant remains	8790 \pm 50	9601-10145	9816
Beta 306675	980	Plant remains	9020 \pm 40	9967-10248	10207
Beta 327103	1005	Plant remains	9580 \pm 40	10741-11121	10934
Beta 327104	1065	Plant remains	10210 \pm 50	11718-12118	11914
Beta 327105	1080	Plant remains	10350 \pm 50	12004-12402	12211

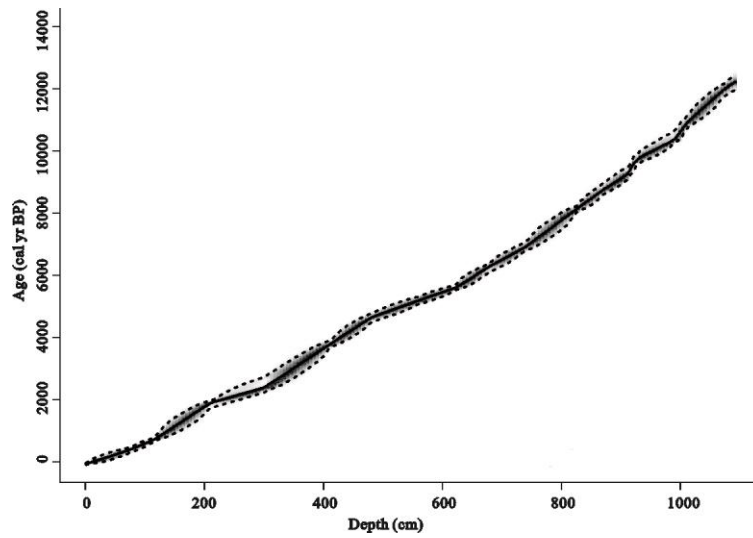
607



608

609 **Fig. 1.** a. Location of Wuxu Lake in monsoonal Asia (yellow triangle) and of the paleoclimate sites
610 mentioned in the text (yellow circles); and the dominant circulation systems of the Indian summer
611 monsoon, East Asian summer monsoon and the East Asian winter monsoon. 1, Moomi Cave (Shakun et
612 al., 2007); 2, Qunf Cave (Fleitmann et al., 2003); 3, Hoti Cave (Fleitmann et al., 2007); 4, Lonar Lake
613 (Prasad et al., 2014; Sarkar et al., 2015); 5, Core SO188-342KL (Contreras-Rosales et al., 2014); 6, Tso
614 Kar (Demske et al., 2009); 7, Tianmen Cave (Cai et al., 2012); 8, Paru Co (Bird et al., 2014); 9,
615 Gonghe Basin (Liu et al., 2013); 10, Gulang profile (Sun et al., 2012); 11, Jingyuan profile (Sun et al.,
616 2012); 12, Naleng Lake (Kramer et al., 2010); 13, Tiancai Lake (Xiao et al., 2014b); 14, Xingyun Lake
617 (Chen et al., 2014); 15, Huguangyan Lake (Jia et al., 2015; Wang et al., 2012); 16, Core MD05-2904
618 (Steinke et al., 2011); 17, Core MD01-2390 (Steinke et al., 2010). b. Expanded view of the study area.

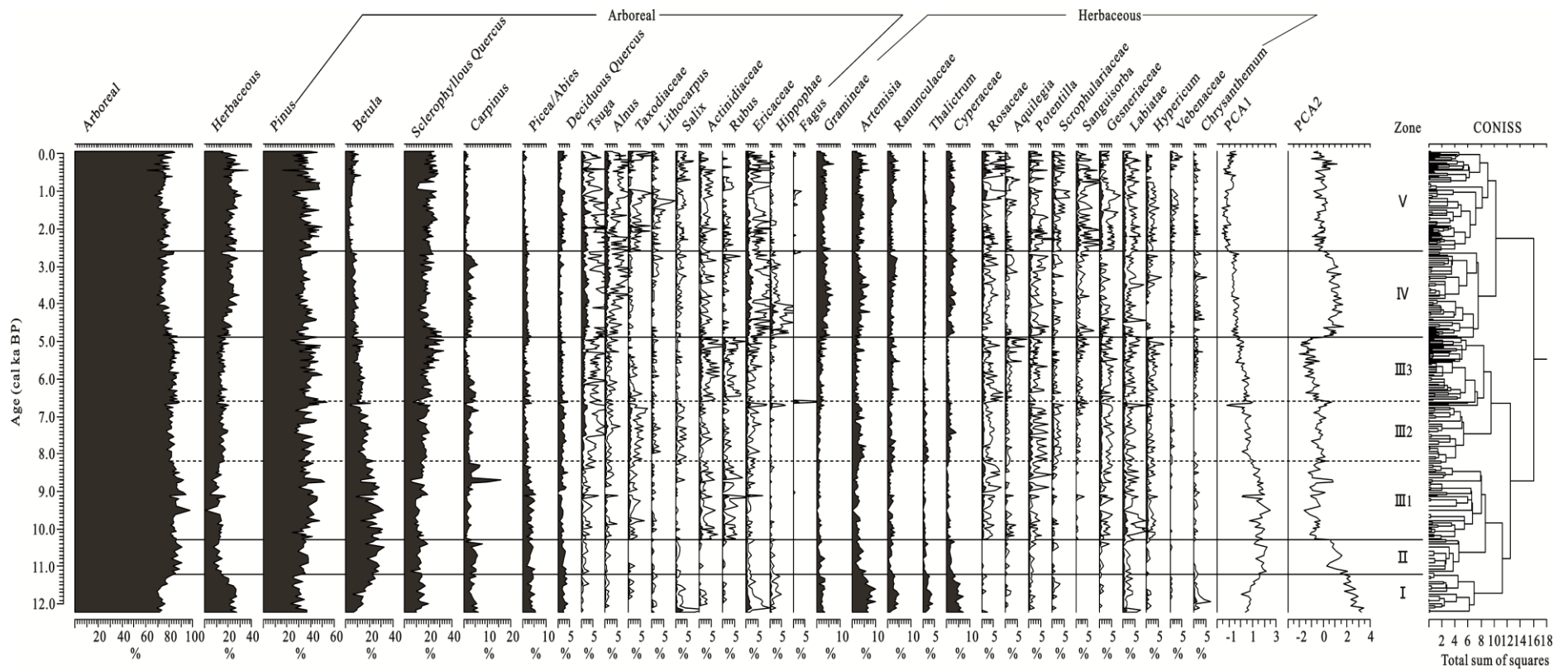
619



620

621 **Fig. 2.** Age-depth model for the Wuxu Lake sediment core produced by Bacon software. The dotted
622 lines indicate the 95% confidence limits and the solid line shows the weighted mean ages for each
623 depth (Blaauw and Andres Christen, 2011; R Development Core Team, 2013).

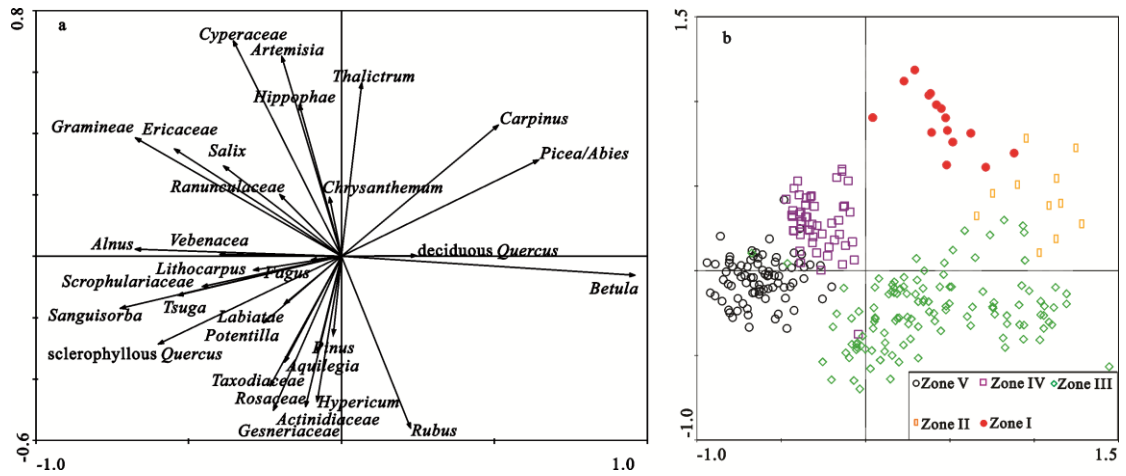
624



625

626 **Fig. 3.** Pollen percentage diagram of selected taxa from the sediment core from Wuxu Lake. Pollen types with relatively low percentages are $\times 5$.

627



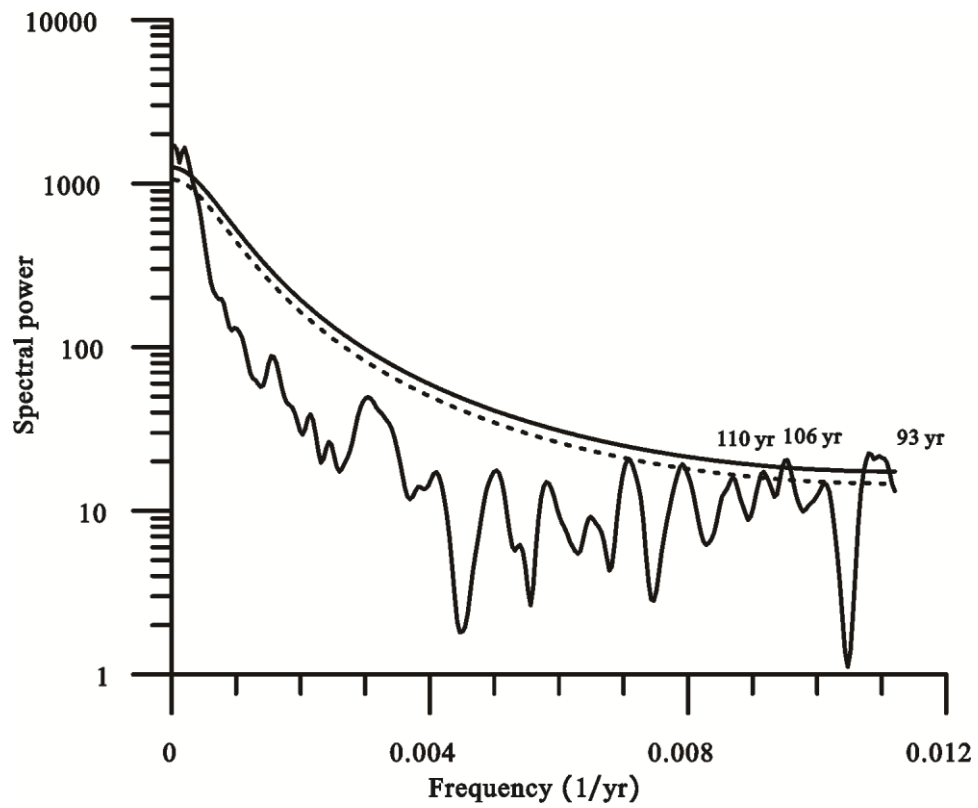
628

629 **Fig. 4.** Results of PCA of the pollen percentage data from Wuxu Lake. (a) Variable loadings on the first two
 630 principal components. (b) Sample scores on the first two principal components.

631

632

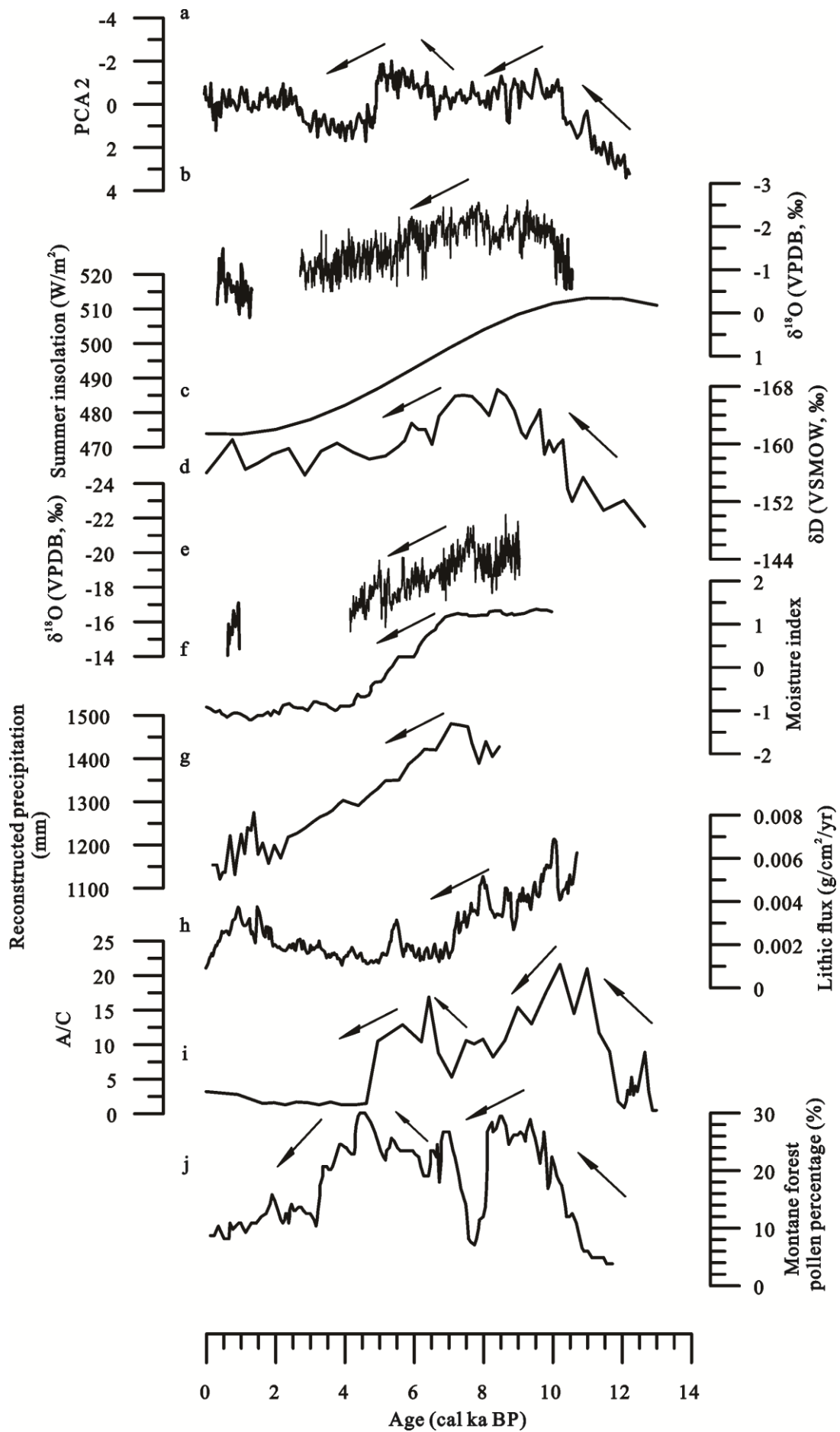
633



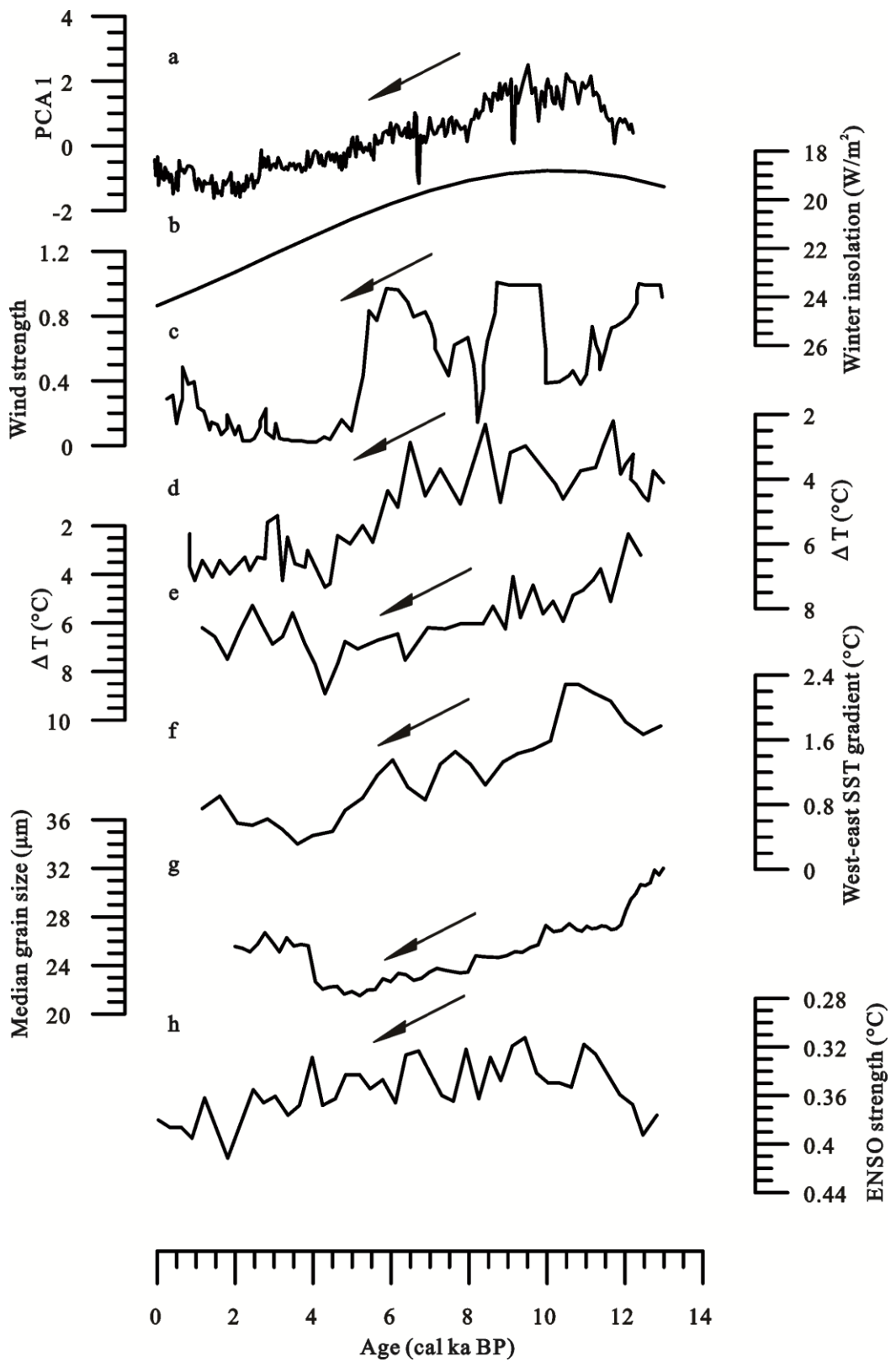
634

635 **Fig. 5.** Results of spectral analysis of the PCA 2 axis sample scores of the pollen record from Wuxu Lake over the
636 past 12.3 ka. Periodicities which exceed the 90% confidence level (dashed line) are labelled. Solid line shows the
637 95% confidence level.

638



640 **Fig.6.** Sample scores on PCA axis 2 of pollen data from Wuxu Lake interpreted as a proxy for precipitation (a) and
641 compared with other paleoclimate records. (b) Speleothem $\delta^{18}\text{O}$ record from Qunf Cave in southern Oman
642 (Fleitmann et al., 2003); (c) June insolation at 30 °N (Berger and Loutre, 1991); (d) hydrogen isotopic record from
643 the northern Bay of Bengal (Contreras-Rosales et al., 2014); (e) speleothem $\delta^{18}\text{O}$ record from Tianmen Cave in the
644 southern QTP (Cai et al., 2012); (f) synthesized Holocene effective moisture index from the ISM region (Wang et
645 al., 2010); (g) annual precipitation reconstructed from pollen assemblages from Xingyun Lake in southwestern
646 China (Chen et al., 2014); (h) record of lithic flux at Paru Co in the southern QTP (Bird et al., 2014); (i) *Artemisia*
647 to *Chenopodiaceae* (A/C) ratio from Tso Kar in the western QTP (Demske et al., 2009); (j) montane forest pollen
648 percentage record from Naleng Lake in the southeastern QTP (Kramer et al., 2010).



649

650

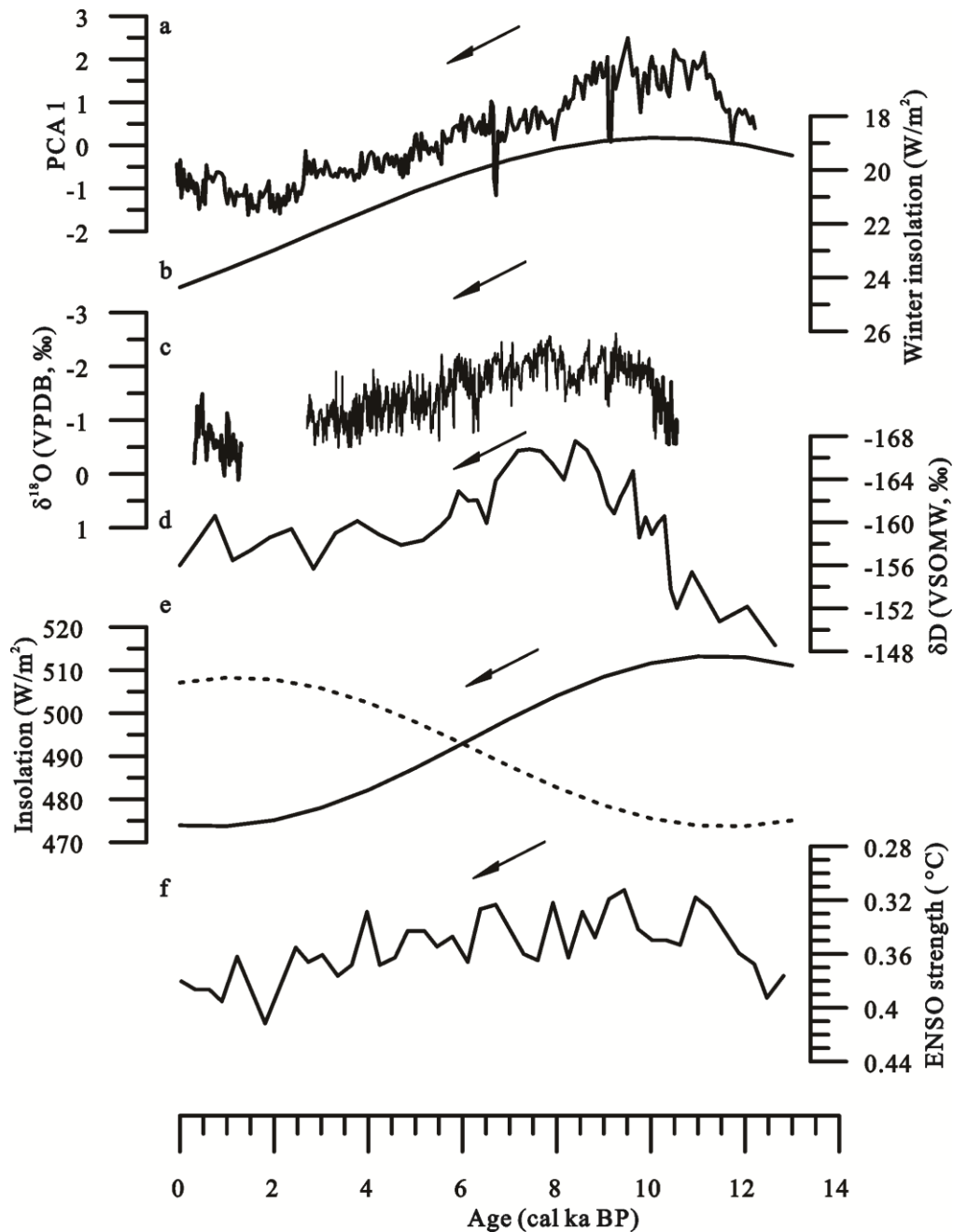
651 **Fig. 7.** Sample scores on PCA axis 1 of pollen data from Wuxu Lake interpreted as a proxy for EAWM (a) and

652 compared with other paleoclimate records. (b) December solar insolation at 60° N (Berger and Loutre, 1991); (c)

653 winter wind strength record from Huguangyan Lake (Wang et al., 2012); (d) record of the Pacific Ocean thermal
654 gradient between the surface and the thermocline from core MD05-2904 (Steinke et al., 2011); (e) record of the
655 Pacific Ocean thermal gradient between the surface and the thermocline from core MD01-2390 (Steinke et al.,
656 2010); (f) west-east SST gradient of the South China Sea (Huang et al., 2011); (g) grain-size record from the
657 Jingyuan loess section (Sun et al., 2012); (h) ENSO amplitude based on a transient Coupled General Circulation
658 Model simulation in 300-year windows (Liu et al., 2014).

659

660



662

663 Fig. 8. Comparison of the EAWM and the ISM based on proxy records. (a) Sample scores on PCA axis 1 of pollen
 664 data from Wuxu Lake; (b) December solar insolation at 60° N (Berger and Loutre, 1991); (c) speleothem $\delta^{18}\text{O}$
 665 record from Qunf Cave in southern Oman (Fleitmann et al., 2003); (d) hydrogen isotope record from the northern
 666 Bay of Bengal (Contreras-Rosales et al., 2014); (e) contrast of solar insolation between 30° N in June (solid line)
 667 and 30° S in December (dashed line) (Berger and Loutre, 1991); (f) record of ENSO amplitude based on a
 668 transient Coupled General Circulation Model simulation in 300-year windows (Liu et al., 2014).